THE JOURNAL OF PHYSICAL CHEMISTRY B

pubs.acs.org/JPCB Article

Imaging Switchable Protein Interactions with an Active Porous Polymer Support

Published as part of The Journal of Physical Chemistry virtual special issue "Time-Resolved Microscopy".

Chayan Dutta, Logan D. C. Bishop, Jorge Zepeda O, Sudeshna Chatterjee, Charlotte Flatebo, and Christy F. Landes*

Cite This: https://dx.doi.org/10.1021/acs.jpcb.0c01807 Read Online

ABSTRACT: Mechanistic details about how local physicochemistry of porous interfaces drives protein transport mechanisms are necessary to optimize biomaterial applications. Cross-linked hydrogels made of stimuli-responsive polymers have potential for active protein capture and release through tunable steric and chemical transformations. Simultaneous monitoring of dynamic changes in both protein transport and interfacial polymer structure is an experimental challenge. We use single-particle tracking (SPT) and fluorescence correlation spectroscopy Super-resolution Optical Fluctuation Imaging (fcsSOFI) to relate the switchable changes in size and structure of a pH-responsive hydrogel to the interfacial transport properties of a model protein, lysozyme. SPT analysis reveals the reversible switching of protein transport dynamics in and at the hydrogel polymer in response to pH changes. fcsSOFI allows us to relate tunable heterogeneity of the hydrogels and pores to reversible changes in the distribution of confined diffusion and adsorption/desorption. We find that physicochemical heterogeneity of the hydrogels dictates protein confinement and desorption dynamics, particularly at pH conditions in which the hydrogels are swollen.

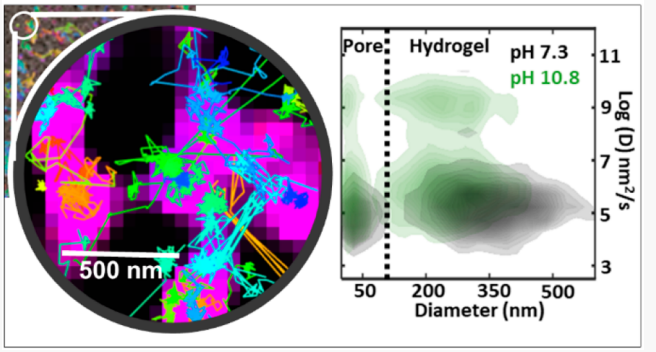

INTRODUCTION

Porous materials have diverse applications ranging from membrane fuel cells[1] and dye-sensitized solar cells in energy applications,[2] mesoporous silica in molecular separations,[3−7] and hydrogels in biomedical sciences.[8−12] The nano- and microscale porous structure of these materials plays a pivotal role in achieving their diverse functionalities. Active soft polymeric materials with environment-sensitive physicochemical properties are ideal for applications such as targeted drug delivery[13] and separations.[14] Currently, biomolecular separation remains an expensive and time-consuming process that could benefit from new active stationary phase supports.[15,16] Such supports could be used in adaptive separation columns for next-generation protein purification. However, future applications require a detailed understanding of the time-dependent changes in the porous structure under ambient conditions and nanoscale control of biomolecular interactions at the polymer surface.

Cross-linked hydrogel nanoparticles made of stimuli-responsive active polymers have attracted considerable attention in several biomedical technology domains including separation and purification of biomolecules.[17−22] Stimuli-responsive hydrogels are attractive due to their spatial and chemical tunability in response to environmental stimuli such as pH, temperature, light, and ionic strength. However, active polymer hydrogels are functionally complex with disordered and heterogeneous nanoporous structures. Localized stimuli-driven transformations of hydrogels generate a dynamic heterogeneity in their physicochemical properties and are the driving forces behind their potential for active separations materials.[23,24] Currently, a single molecule understanding of interfacial protein dynamics and transport within nanopores is lacking.

Electron and force microscopy methods, such as scanning electron microscopy (SEM), transmission electron microscopy (TEM), and atomic force microscopy (AFM) require extreme conditions that distort or destroy the porous structure.[25] Ensemble techniques (such as X-ray diffraction) are useful for nanoscale chemical details but can mask the effects of nano-

Received: February 29, 2020
Revised: April 24, 2020
Published: May 12, 2020

and microscale heterogeneity.[26] Microrheological measurements of viscoelastic properties by tracer particle tracking require high computational cost and lack spatial resolution.[27] Super-resolution fluorescence microscopy techniques have been applied for the elucidation of nanoscale properties of various soft polymer materials.[28,29] Three-dimensional structures of block copolymers and polymers blends have been studied using various forms of stimulated emission depletion (STED) microscopy,[30−32] localization-based photoactivated localization microscopy (PALM)[33,34] and stochastic optical reconstruction microscopy (STORM).[35−41]

In the present work, we use single-particle tracking (SPT)[42] and fluorescence correlation spectroscopy Super-resolution Optical Fluctuation Imaging (fcsSOFI)[43] to characterize the porous structure and diffusion properties of allylamine functionalized poly-*N*-isopropylacrylamide (pNIPAM-*co*-AA) pH-sensitive hydrogels. SPT analysis of lysozyme interaction on the hydrogel surface reveals the dynamic reversibility of the hydrogel polymer in response to the pH change of the environment. fcsSOFI analysis provides diffusion maps of the hydrogel surface in confined conditions. Our results suggest that slower, confined motion at neutral pH is the dominant mode of transport at these hydrogel surfaces under ambient conditions. We also demonstrate the reversible tunability of single protein interfacial dynamics at these surfaces, which is an essential first step toward understanding variable structure−function relationships of functional active materials for predictive applications.

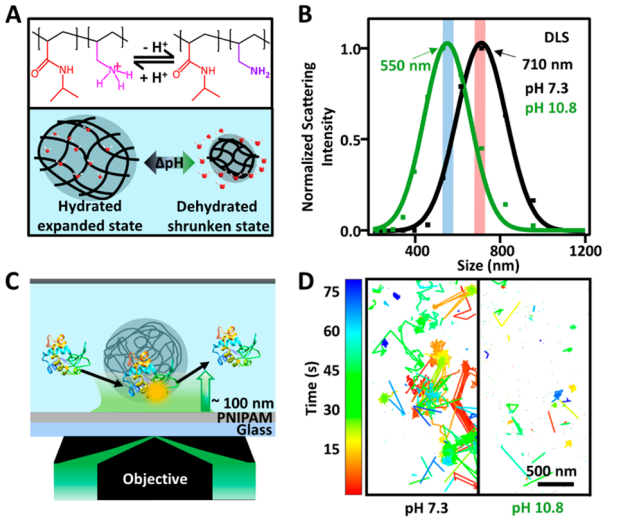

Figure 1. SPT analysis of lysozyme dynamics at pH-responsive poly(*N*-isopropylacrylamide-*co*-allylamine) (PNIPAM-*co*-AA) hydrogel surface. (A) Unit molecular structure (top panel) and cartoon representation (bottom panel) of the pH response for PNIPAM-*co*-AA hydrogels. (B) Size of synthesized PNIPAM-*co*-AA hydrogels at pH 7.3 and at pH 10.8 measured with DLS. (C) Schematic of the sample chamber used for widefield microscopy in TIRF mode excitation. (D) Representative time-dependent lysozyme trajectories at the PNIPAM-*co*-AA surface at pH 7.3 and at pH 10.8.

EXPERIMENTAL SECTION

Materials and Methods. *Hydrogel Preparation.* *N*-Isopropylacrylamide (≥99%, Sigma-Aldrich), *N*,*N*′-methylenebis(acrylamide) (99%, Sigma-Aldrich), allylamine (≥99%, Sigma-Aldrich), potassium persulfate (99%, ACROS Organics), and poly-NIPAM (pNIPAM) (Polysciences) were purchased and used as received. pNIPAM-*co*-AA hydrogels were synthesized by free-radical polymerization following the procedure by Lim et al.[44] *N*-Isopropylacrylamide (0.25 g) and *N*,*N*′-methylenebis(acrylamide) (0.011 g) were dissolved in 50 mL of deionized (DI) water at room temperature. The solution was degassed under nitrogen for 30 min and then heated to 80 °C. Allylamine (70 μL) and aqueous potassium persulfate (2 mL, 0.025 g/mL) were added to the reaction consecutively. The persulfate solution was degassed under nitrogen for 10 min before adding to the reaction. The reaction proceeded for 2 h at 80 °C; then the hydrogels were purified via centrifugation and redispersed in DI water.

Protein Preparation. Rhodamine B labeled lysozyme C (Nanocs) solutions (0.5 nM) were freshly prepared in HEPES (pH 7.3) and Tris (pH 10.8) buffer. Buffers were prepared at 10 mM concentrations using HEPES (Sigma) and Tris ($[CH_2OH]_3CNH_2$) (Fischer Scientific) and the pH was measured on a Thermo Scientific Orion 2 Star pH meter.

Dynamic Light Scattering (DLS) and Zeta Potential (ζ) Measurements. Hydrogel particle size was measured using a Zetasizer nanoscale light scattering instrument (Malvern Instruments, Zen 3600 Nanoseries) at pH 7.3 and pH 10.8. All measurements are taken at 25 °C after 2 min equilibration in the instrument. The unit molecular structure of the pNIPAM-*co*-AA polymer and the pH response of the hydrogels are presented in Figure 1A. Experimentally measured sizes of the synthesized hydrogels at pH 7.3 and pH 10.8 are presented in Figure 1B. The ζ potentials of the hydrogels and lysozyme at both pH conditions were also measured and presented in Figure S1 in the Supporting Information.

Scanning Electron Microscope (SEM) Characterization of Hydrogels. The pNIPAM hydrogels were imaged with a SEM (FEI Helios 660 NanoLab DualBeam, 5 kV and 25 pA) on indium tin oxide supports (Evaporated Coatings Incorporated, 55 ohm/sq). The conductive support was oxygen plasma-cleaned for 2 min and the hydrogels were spin-cast on the plasma-cleaned surface. SEM images are presented in Figure S2 in the Supporting Information.

Circular Dichroism (CD) Spectroscopy. Protein secondary structure data were obtained using a JASCO J-810 spectropolarimeter. Measurements of each solution were conducted at room temperature from wavelengths of 190−250 nm with a scan speed of 20 nm/min in a 0.01 cm quartz cuvette. Data were obtained in millidegrees and averaged over 10 accumulations with a data pitch of 0.1 nm. Millidegrees were converted into molar residue ellipticity ($[\theta]$) using the equation $[\theta] = \frac{\theta}{10 \times l \times N \times c}$, where θ is the ellipticity in degrees reported by the instrument, l is the path length of the cuvette in cm, N is the number of residues in the protein, and c is the concentration of the protein in g/cm^3.

Wide-Field Single-Molecule Fluorescence Imaging. Single-molecule fluorescence measurements were performed on a home-built wide-field microscope (Figure 1C) in total internal reflection fluorescence (TIRF) excitation that has been previously reported.[45] Briefly, a continuous-wave circularly polarized 532 nm laser (Coherent) was used as an excitation source. A 100× NA 1.45 oil-immersion objective (alpha Plan-Fluar, Carl Zeiss) was used to focus the excitation beam onto the sample surface in epi-mode. Single-molecule data were collected from a 256 × 256 pixel (16 μm × 16 μm) area on the sample surface, where one pixel corresponds to 64 nm. The power density used in all experiments was 0.10 kW/cm^2 at the

https://dx.doi.org/10.1021/acs.jpcb.0c01807
J. Phys. Chem. B XXXX, XXX, XXX−XXX

interface. The fluorescence signal from the tagged protein molecules was collected through the same objective and imaged by an EMCCD camera (Andor, iXon 897) after passing through an excitation notch filter (Kaiser, HNPF-532-1.0) and an emission bandpass filter (Chroma, ET585/65m). The camera was operated in frame transfer mode and controlled by the Andor Solis software with an image acquisition time of 15 ms. The imaging area was illuminated by the 532 nm laser (power density 0.25 kW/cm^2) for at least 20 min to photobleach contaminants prior to single-molecule experiments.

Sample Preparation for Microscopy Experiments. Microscope coverslips (22 × 22 mm, no. 1; VWR) were sequentially sonicated for 5 min in DI water, ethanol, and acetone. Coverslips were then immersed in base piranha for 20 min at 80 °C. After thorough rinsing with DI water, the coverslips were treated with oxygen plasma for 2 min (PDC-32G; Harrick Plasma, Ithaca, NY). A dilute solution (100 μL, 2% w/w) of pNIPAM was spin coated on the clean glass coverslips and was used as blank control samples. As the refractive index of the polymer is similar to that of glass (∼1.52),[46] the TIRF condition at the pNIPAM/water interface is maintained as presented schematically in Figure S3 in the Supporting Information. Synthesized pNIPAM-*co*-AA hydrogels were spin coated on top of the pNIPAM film for protein interaction on the hydrogel experiments. The surface of each of the samples was enclosed inside a hybriwell chamber (Grace BioLabs). Protein solutions at different pH buffer were continuously flowed through the enclosed chamber at a rate of 10 μL/min and allowed to equilibrate for at least 15 min before data acquisition.

Data Analysis. *SPT Analysis.* Single protein tracking on the hydrogel surface was performed using a Matlab particle identification and tracking algorithm previously developed by Shuang el al.[42] This algorithm executes three sequential steps on the raw single-molecule data sets. Matlab compatible raw data sets obtained from the Andor video files were processed frame by frame and the signal-to-noise ratio is increased by applying a 3 by 3 pixel averaging matrix. Then, a particle identification routine identifies protein molecules by local intensity maximum and determines the center position by radial symmetry fitting.[47] Finally, the molecular trajectories are connected for all detected molecules using a nearest neighbor algorithm. Representative time-dependent trajectories obtained from SPT analysis for lysozyme interacting with the pNIPAM-*co*-AA hydrogels at pH 7.3 and pH 10.8 are presented in Figure 1D.

Radius of Gyration Analysis. Trajectory motion was analyzed using the logarithm of each trajectory's radius of gyration (R_g).[48−50] R_g is calculated as the root-mean-square distance (in pixels) from the first point localized in the trajectory. Mathematically, this is

$$R_g = \sqrt{R_1^2 + R_2^2} \tag{1}$$

where R_1 and R_2 are the major and minor eigenvalues of the radius of gyration tensor. This tensor takes the following form

$$\begin{pmatrix} \frac{1}{N}\sum_{j=1}^{N}(x_j - \langle x\rangle)^2 & \frac{1}{N}\sum_{j=1}^{N}(x_j - \langle x\rangle)(y_j - \langle y\rangle) \\ \frac{1}{N}\sum_{j=1}^{N}(x_j - \langle x\rangle)(y_j - \langle y\rangle) & \frac{1}{N}\sum_{j=1}^{N}(y_j - \langle y\rangle)^2 \end{pmatrix} \tag{2}$$

where x_j and y_j are the x and y coordinates of the jth point and N is the total number of points in the trajectory. R_g describes the area covered by a molecule across the entire measured trajectory and is beneficial when trajectories exhibit non-Brownian diffusion.[49] We have used $\log_{10} R_g < 0$ to quantify the number of confined particles, which represents the dynamics of particles confined within a pixel (1 pixel = 64 nm). Conversely, particles that are moving across the field of view have $\log_{10} R_g > 0$. The asymptotic line at 0 then becomes a binary divider describing molecules captured within the hydrogels and those traveling across the surface.

fcsSOFI Analysis. Super-resolution diffusion maps of the pNIPAM-*co*-AA hydrogel surface were obtained by correlation based fcsSOFI technique.[43] The second-order autocorrelation of the stochastic optical fluctuation of independently diffusing emitters at the surface or within the hydrogel pores is given by

$$G_2(r,\tau) \sim \int \mathrm{d}r_1\, U(r-r_1) \times \left[U(r - r_1) \otimes \exp\left(-\frac{(r - r_1)^2}{4D\tau}\right)\right]\epsilon_1^2 \tag{3}$$

where $U(r-r_1)$ is the point spread function (PSF) centered at r_1, D is the diffusion coefficient, τ is the time lag, ε_1 is the constant brightness of the emitter, and ⊗ stands for convolution. Assuming a Gaussian PSF, the second-order autocorrelation provides 2D resolution enhancement for fcsSOFI from diffraction-limited images. However, the resolution enhancement is limited due to fast diffusing emitters and the enhancement is always below the SOFI limit.[43,51] Distributions of the diffusion coefficients were obtained from fits of the correlation curves. Curve fitting over all time lags was performed for the calculated $G_2(r,\tau)$ at each pixel assuming confined motion using,

$$G_2(r,\tau) = A(r)\frac{1}{1 + \left(\frac{\tau}{\tau_D}\right)^{\alpha}} + c \tag{4}$$

where $A(r)$ is the amplitude $G_2(r,0)$, τ_D is the characteristic diffusion time at that pixel, α is the subdiffusion coefficient and c is a constant offset. For Brownian diffusion processes, α is equal to 1. For anomalous confined diffusion or subdiffusive motion α is less than 1, and for superdiffusive or motion under external forces α is greater than 1. Diffusion coefficients were set to zero if the R^2 of the fit was less than 0.5. The diffusion coefficient (D) of the emitter can be approximated by assuming a two-dimensional motion[52] of the emitter as

$$D = \frac{\omega^2}{4\tau_D} \tag{5}$$

where ω is the size of the detection region which is a combination of the pixel size and the microscope PSF. D and α values are obtained from each pixel for the entire region of

https://dx.doi.org/10.1021/acs.jpcb.0c01807
J. Phys. Chem. B XXXX, XXX, XXX−XXX

interest. fcsSOFI analysis was performed on the single-molecule data sets acquired for the SPT analysis on the same field of view for both pH conditions.

The super-resolution diffusion map was generated by fusing the spatial and diffusion results on a HSV colormap.[43] The hue (H) is the normalized log of D, the saturation (S) is the normalized super-resolution spatial information and the value (V) is set to a constant value of 1. Converting the HSV matrix to RGB creates an image that contains both the diffusion map and the super-resolution image of the hydrogel.

Hydrogel size identification from the fcsSOFI maps was performed using nonmaximum suppression seeded K-means clustering.[53] Hydrogel centers were identified by locating intensity peaks in the super-resolution map through non-maximum suppression within a 3 pixel radius. The super-resolution map was binarized above two standard deviations of the mean background intensity to extract pixels that corresponded to hydrogel structures. The background intensity was determined from a 35 × 35 pixel region without a hydrogel in the fcsSOFI image. If a previously identified hydrogel structure was not present in the binarized image, it was discarded. The identified hydrogel centers then served as the centroid initialization in K-means clustering. By seeding K-means, we ensured reproducibility[54,55] and optimal clustering performance.[55−58] K-means then classified each pixel in the binarized image according to the nearest seeded cluster center. The area of each hydrogel is proportional to the number of pixels contained in each cluster.

Single-molecule trajectories obtained from SPT analysis were further analyzed by searching for confined subtrajectories to obtain pore sizes. A minimal spanning tree links together clusters of points in each trajectory corresponding to instances of confined motion connected by jumps. We removed connections between clusters greater than one pixel to isolate regions of confined motion into subtrajectories. Subtrajectories shorter than the frame tolerance were discarded. A frame tolerance of 0.06 s (4 frames) was selected to ensure reliable dynamics information. The pore size was then estimated by performing radius of gyration analysis on each subtrajectory.

RESULTS AND DISCUSSION

Lysozyme Desorption Dynamics. Lysozyme desorption dynamics on the pNIPAM-*co*-AA surface are reversible as a function of pH (Figure 2). Surface residence time (SRT) analyses show the number of distinct populations of lysozyme desorption from the hydrogel surface. Cumulative distributions of SRT for lysozyme at pH 7.3 and pH 10.8 are calculated from the single-molecule trajectories obtained from SPT analysis by calculating the amount of time a molecule remains at the surface. The SRT decays faster at pH 10.8 than at pH 7.3, which shows that long-lived trajectories are more prevalent at pH 7.3. SRT distributions at these two pH conditions measured for six consecutive cycles from the same area are presented in Figure 2A. The SRT is switched back and forth for multiple cycles in these two pH conditions, demonstrating a reversible change in surface properties for the hydrogels, as shown in Figure 2B. Decay curves are fit with three exponentials assuming first-order kinetics using eq 6

$$P(t>t_0) = \sum_{i=1,2,3} \beta_i \exp\left(-\frac{t}{\tau_i}\right) \quad (6)$$

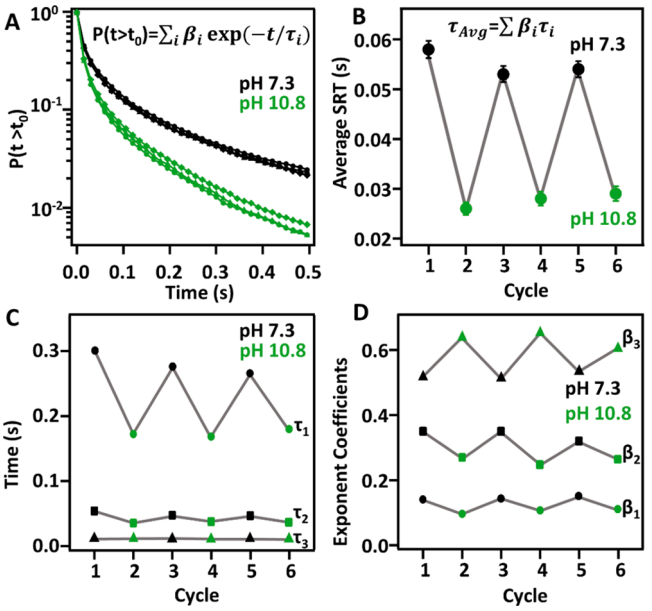

Figure 2. pH controls the surface residence times of lysozyme reversibly. (A) Cumulative SRT distribution of lysozyme at PNIPAM-*co*-AA surface at pH 7.3 and pH 10.8 for 6 cycles. (B) Average surface residence time at pH 7.3 and pH 10.8 for each cycle, showing the reversibility in the average time lysozyme stays at the surface. (C) Time constants and (D) pre-exponential coefficients obtained from exponential fitting of the cumulative SRTs at pH 7.3 and pH 10.8 also showing reversible change.

where β_i is the pre-exponential coefficient with the characteristic residence time τ_i. Two-component fits of the decay curves were insufficient in providing a good quality fit as presented in Figure S4 in the Supporting Information. Average SRT's are calculated as the weighted averaged sum ($=\Sigma\beta_i\tau_i$) of all three components and plotted in Figure 2B for all cycles. All fitting parameters are presented below in Table 1. Average SRT values are reversible in response to pH and show that lysozyme stays at the surface longer at neutral pH. Curve fitting of the cumulative decay curves also provides the individual kinetic parameters for each subpopulation. Individual residence times (τ_i) and the associated pre-exponential coefficients (β_i) are plotted in Figure 2C,D, respectively. All parameters are reversible as a function of pH. Time scales (τ_1 and τ_2) for the slower subpopulations associated with surface diffusion switch from a higher value at pH 7.3 to a lower value at pH 10.8. The corresponding populations (β_1 and β_2) also change between higher and lower values as the pH cycles. The fastest time component, τ_3, does not change. The most likely explanation is that this component corresponds to reversible

Table 1. SRT Distribution Fitting Parameters:

	cycle 1		cycle 2		cycle 3	
	pH 7.3	pH 10.8	pH 7.3	pH 10.8	pH 7.3	pH 10.8
β_1	0.125	0.079	0.128	0.089	0.136	0.093
τ_1 (s)	0.297	0.169	0.272	0.164	0.261	0.176
β_2	0.349	0.263	0.35	0.239	0.316	0.256
τ_2 (s)	0.05	0.032	0.043	0.034	0.043	0.033
β_3	0.526	0.658	0.522	0.672	0.547	0.621
τ_3 (s)	0.008	0.008	0.008	0.007	0.008	0.007
τ_{avg} (s)	0.058	0.026	0.053	0.028	0.054	0.029

https://dx.doi.org/10.1021/acs.jpcb.0c01807
J. Phys. Chem. B XXXX, XXX, XXX−XXX

adsorption with kinetics that are within the camera frame time (0.015 s) when quantified by ensemble residence time analysis. β_3 reversibly changes with pH, with the trend suggesting that the number of proteins undergoing fast adsorption−desorption is reduced at neutral pH. Control experiments (Figure S5 in the Supporting Information) show that the average SRTs are not affected by the change in laser power and thus photobleaching of the fluorescent dyes does not contribute to the measured residence times. Because of the heterogeneity in surface dynamics, more detail about the types of motion can be revealed by single protein tracking analyses, as discussed below.

Classifying Dynamics from SPT. Confined diffusion of lysozyme at the pNIPAM-*co*-AA hydrogel surface dominates at neutral pH (Figure 3). Radius of gyration (R_g), calculated as

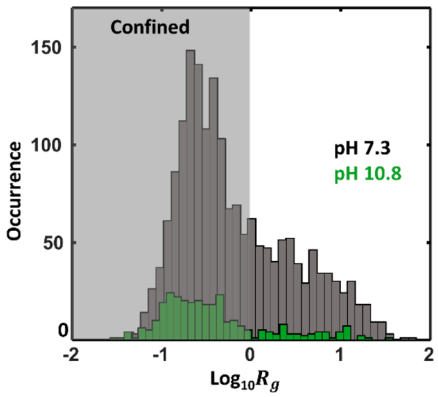

Figure 3. Confined diffusion dominates at neutral pH. Histogram of $\log R_g$ for each condition, where R_g is in pixels and 1 pixel = 64 nm. Trajectory motion was analyzed using the logarithm of each trajectories radius of gyration (R_g). Trajectories with $\log R_g < 0$ represent confined particles (shaded region).

the root-mean-square from the first point localized in each trajectory, is presented in Figure 3, showing the extent of confinement at each condition. An increase in the confined population at pH 7.3 points to more proteins confined in the swollen hydrogels. The number of long-lived confined interactions is almost 10 times higher at pH 7.3 than at pH 10.8, as presented in Figure S6.

Chemical changes in the protein or polymer surface in response to the external pH fail to explain the observed changes in adsorption/desorption dynamics of lysozyme at the hydrogel surface. Adsorption is dictated by long-range electrostatic interaction;[59,60] however, the overall rate of adsorption of lysozyme at the pNIPAM-*co*-AA interface does not change under these pH conditions (Figure S7). Desorption is controlled by short-range noncovalent interactions, such as van der Waals, hydrophobic interactions, and hydrogen bonding.[59] Hence, the desorption rate on the chemistry of these surfaces is not expected to be affected by pH, contrary to what we observe in the present study (Figure 2B). Also, the protein secondary structure does not change in the presence of the hydrogels (Figure S8). Hence, to understand the observed dynamics, we used fcsSOFI analysis to relate the pH-dependent physical changes in the hydrogel structure to the local protein transport properties, as explained in the next section.

Hydrogels Mapped by fcsSOFI. fcsSOFI analysis provides super-resolved maps of lysozyme diffusion dynamics within the hydrogels (Figure 4) and demonstrates how hydrogel size influences transport. The fcsSOFI analysis was

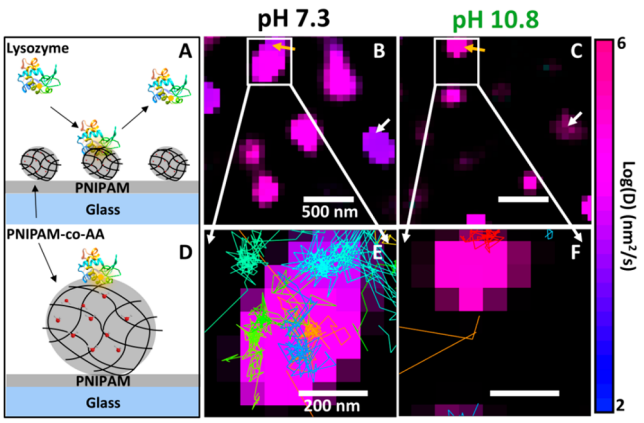

Figure 4. Representative super-resolution fcsSOFI diffusion maps of pNIPAM-*co*-AA hydrogels at each condition. (A) Cartoon representation (side view) of the sample surface with pNIPAM-*co*-AA hydrogels dispersed on a thin layer of pNIPAM. Super-resolution fcsSOFI diffusion maps of pNIPAM-*co*-AA hydrogel surface at pH 7.3 (B) and pH 10.8 (C). Yellow and white arrows in panels B and C point to the same area of the sample surface, showing different hydrogel size and diffusion behavior at different pH conditions. Results are for 0.5 nM lysozyme diffusion at the pNIPAM-*co*-AA surface. (D) Zoomed-in cartoon of one hydrogel interacting with a fluorescently tagged lysozyme protein. (E, F) Zoomed-in fcsSOFI images overlain with the corresponding single-molecule trajectories for one hydrogel at pH 7.3 and 10.8, respectively.

performed on the hydrogels for the entire field of view (16 μm × 16 μm) for multiple samples, and the fcsSOFI images presented in Figure 4 are representative and magnified to clearly show the diffusion heterogeneity within hydrogels. Parts A and D of Figure 4 show cartoon representations of pNIPAM-*co*-AA hydrogels on top of a thin layer of pNIPAM polymer and a zoomed-in view of a fluorescently tagged lysozyme protein interaction with a hydrogel, respectively. fcsSOFI diffusion maps of protein interactions at multiple hydrogel surfaces at both pH 7.3 and pH 10.8 are presented in Figure 4B,C, respectively. The physical dimension of a hydrogel particle at equilibrium is a balance between the osmotic pressure and the polymer elasticity.[61] Protonated amine groups attract hydrated counterions inside the hydrogel, which leads to the swelling of the gel at neutral pH. The expansion provides more space for proteins to explore inside at pH 7.3. A closer look at representative hydrogel nanoparticles (yellow and white arrows in Figure 4B,C) at both pH conditions reveals that the overall size of the hydrogel is larger at pH 7.3, but the distribution of diffusion coefficients observed within each hydrogel also switches with pH 7.3. Figure S9 shows the corresponding autocorrelation curves and R^2 fitting at these locations for both pH conditions.

The heterogeneous transport within each hydrogel is tunable by pH. Parts E and F of Figure 4 show a zoomed-in fcsSOFI image with the corresponding single-molecule trajectories overlain for the same hydrogel at pH 7.3 and pH 10.8, respectively. The heterogeneity in physicochemical properties for the hydrogels in response to varying pH conditions and the variable interaction with the protein is apparent from different diffusion coefficients at the same location. Histogram distributions (Figure S10 and Figure S11) of $\log(D)$ and α

https://dx.doi.org/10.1021/acs.jpcb.0c01807
J. Phys. Chem. B XXXX, XXX, XXX−XXX

show differences in lysozyme diffusion at these pH conditions. Specifically, a higher population of molecules show slow and confined diffusion at pNIPAM-*co*-AA hydrogels at pH 7.3 vs at pH 10.8 (Figure S10A, B). The confined behavior of lysozyme at the pNIPAM-*co*-AA hydrogels is reversible with respect to the pH of the solution (Figure S10). Comparison with SPT analysis demonstrates that, as has been shown previously, SPT in nanoconfined samples can lead to incorrect spatial and diffusion information, whereas fcsSOFI provides super-resolved structural details under confined dimensions.[43] Control samples with only a thin layer of pNIPAM without hydrogels exhibit negligible interactions with lysozyme, as shown in Figure S12. Representative trajectories showing the few nonspecific interactions for the same data obtained from SPT analysis are plotted in Figure S13 in the Supporting Information.

Relationship between Protein Diffusion, Hydrogel Size, And Pore Size. Structural heterogeneity within the hydrogels at the two pH conditions is revealed by statistical analysis of the hydrogel size and diffusion coefficients from the fcsSOFI images (Figure 5). Hydrogel identification and clustering are performed on fcsSOFI maps, as shown for representative hydrogels in Figure 5A, B for pH 7.3 and pH 10.8, respectively. K-means clustering[53] estimates the hydrogel contours, as described in the Experimental Section. The contribution of each pixel toward the hydrogel size is found by using smooth intensity averaging, as presented in Figure S14 in the Supporting Information. The maps in Figure 5A, B confirm that at higher pH the hydrogels shrink, thereby tuning the distribution of protein dynamics. It is important to note that hydrogel sizes calculated by this analysis are much smaller than those obtained by ensemble DLS measurements in solution presented in Figure 1B. It is important to discuss the multiple contributors to the smaller hydrogel sizes calculated by this analysis in comparison to those obtained by ensemble DLS measurements presented in Figure 1B. First, the DLS measurements in solution report the solvated size of the hydrogels, which includes their larger hydration shells. fcsSOFI analysis maps the physical size explored by the protein and is insensitive to the surrounding hydration shell. Next, as has been described elsewhere,[62] the average size of heterogeneous mixtures that is calculated by ensemble methods such as DLS and traditional FCS is nonlinearly shifted when even very small concentrations of larger dissolved species are present because of their relative brightness. Thus, it is expected that DLS measurements overestimate the hydrogel size because of their size heterogeneity. Finally, it is possible that the hydrogels partially collapse on the surface leading to a smaller size for the proteins to explore. Contour plots in Figure 5C detail how the distribution of hydrogel sizes, pore sizes, and log(D) values for protein diffusion switch for each pH condition. A fast diffusing population is observed at pH 10.8 (Figure 5C) within small spaces corresponding to the fast desorbing molecules representing fluctuation in the axial plane with respect to the hydrogel sample surface. A small number of proteins (less than 5%) show fast diffusion at pH 7.3 (Figure S11). We should note here that this fast diffusion of lysozyme at the hydrogels is rather surprising. However, very low signal-to-background due to fast axial motion of molecules contribute to a higher degree of error in measuring the fast diffusion component. Further study, and perhaps simulations, are needed to understand the mechanism of this motion. As shown in Figure 5D, long trajectories show strong confinement in the collapsed hydrogels. This observation further supports the model that short-lived fast desorbing molecules are captured in our fcsSOFI analysis at pH 10.8. The normalized pore diameter distributions for both pH conditions are compared as a histogram in Figure S15 in the Supporting Information.

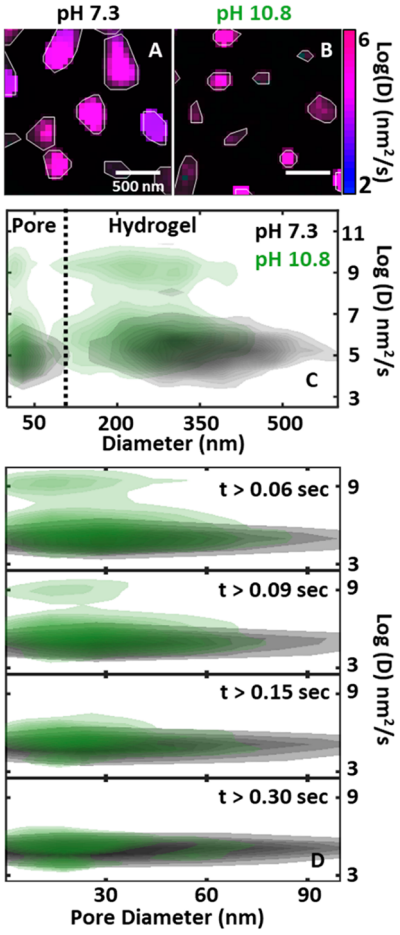

Figure 5. Hydrogel size distribution and diffusion coefficients. Representative fcsSOFI maps of hydrogels and the hydrogel pores identified by K-means clustering method at pH 7.3 (A) and pH 10.8 (B), respectively. Each identified hydrogel in the fcsSOFI map has been circled on the image for better visualization. (C) Contour plots of the hydrogel diameters, estimated pore diameters, and log(D) values for all hydrogels. (D) Distributions separated by length of trajectory, showing collapse of log(D) for long trajectories.

CONCLUSION

We provide molecular insight into the switchable diffusion dynamics of proteins in an active porous medium. We used pH-responsive pNIPAM-*co*-AA hydrogels as an active surface and controlled the dynamics of a model protein at the single-molecule level. Our results suggest that lysozyme shows variable surface interaction with the hydrogel surface at pH conditions below and above the point of zero charge of the hydrogel (pH ~ 9.5). These interactions between the protein and the polymer surface are reversible with respect to the change in the pH of the environment. We have also demonstrated that the super-resolution fcsSOFI technique can be implemented to understand the structural heterogeneity of the hydrogels as well as diffusion properties at various pH conditions. Slower and confined diffusion dominates at neutral

https://dx.doi.org/10.1021/acs.jpcb.0c01807
J. Phys. Chem. B XXXX, XXX, XXX−XXX

pH (pH 7.3), suggesting a higher number of protein molecules exploring larger space as hydrogels swell. A fast diffusing confined population arises due to the fluctuation of the emitters in the axial plane. The pore diameter of the hydrogels calculated from the confined subtrajectories also shows smaller pores at pH 10.8 with a fast diffusing protein molecule. Our studies suggest that biological transport is dictated by the porous confinement of the active hydrogel material and controlling physicochemical interaction at the nanoscale can control the transport dynamics. It is important to note that the present data map three-dimensional dynamics onto a two-dimensional diffusion map. As the experiments were performed in widefield TIRF excitation, only the subset of dynamics within the evanescent field decay (~200 nm or less) from the surface are captured in our analysis. It is important to characterize structural heterogeneity and diffusion properties in three dimensions. Hence, future efforts that combine three-dimensional imaging with point spread function engineering[63−65] and fcsSOFI are necessary.

■ ASSOCIATED CONTENT

Supporting Information

The Supporting Information is available free of charge at https://pubs.acs.org/doi/10.1021/acs.jpcb.0c01807.

Zeta potential (ζ) measurements of pNIPAM-*co*-AA hydrogels and lysozyme, SEM images of the hydrogels on the ITO surface, TIRF condition at the pNIPAM film/water interface, three exponential fit vs two exponential fit of the cumulative SRT distributions, influence of laser power on the surface residence time, number of long-lived events vs pH, rate of adsorption of lysozyme at the hydrogels, electrostatic distribution and structure of lysozyme at different pHs, autocorrelation curve fitting from fcsSOFI, distribution of diffusion coefficients and subdiffusion coefficients from fcsSOFI analysis, comparison of fcsSOFI maps and particle trajectories for lysozyme interaction on the hydrogel surface and on the pNIPAM polymer surface, trajectories of lysozyme interaction on the hydrogel surface and on the pNIPAM polymer surface, background and intensity threshold for hydrogel identification, and pore size distribution and the corresponding diffusion coefficient with varying length of the trajectories (PDF)

■ AUTHOR INFORMATION

Corresponding Author

Christy F. Landes − *Department of Chemistry, Department of Electrical and Computer Engineering, and Department of Chemical and Biomolecular Engineering, Rice University, Houston, Texas 77005, United States;* orcid.org/0000-0003-4163-6497; Phone: (713) 348-4232; Email: cflandes@rice.edu

Authors

Chayan Dutta − *Department of Chemistry, Rice University, Houston, Texas 77005, United States;* orcid.org/0000-0003-4839-2245

Logan D. C. Bishop − *Department of Chemistry, Rice University, Houston, Texas 77005, United States;* orcid.org/0000-0003-2265-4374

Jorge Zepeda O − *Department of Electrical and Computer Engineering, Rice University, Houston, Texas 77005, United States*

Sudeshna Chatterjee − *Department of Chemistry, Rice University, Houston, Texas 77005, United States;* orcid.org/0000-0001-8733-0587

Charlotte Flatebo − *Department of Chemistry and Applied Physics Program, Rice University, Houston, Texas 77005, United States*

Complete contact information is available at: https://pubs.acs.org/10.1021/acs.jpcb.0c01807

Notes

The authors declare no competing financial interest.

■ ACKNOWLEDGMENTS

C.D., J.Z.O, S.C., and C.F.L. thank the National Science Foundation (grant no. CHE-1808382) and the Welch Foundation (grant no. C-1787), L.D.C.B. acknowledge that this material is based upon work supported by the National Science Foundation Graduate Research Fellowship Program (Grant 1842494), C.F. acknowledges support from the National Defense Science and Engineering Graduate Fellowship. This work was concluded in part using resources of the Shared Equipment Authority (SEA) at Rice University. The authors thank all the members of the Landes research group, Prof. Stephan Link, and his research group for helpful discussions.

■ REFERENCES

(1) Wang, X.; Zhang, H.; Zhang, J.; Xu, H.; Tian, Z.; Chen, J.; Zhong, H.; Liang, Y.; Yi, B. Micro-Porous Layer with Composite Carbon Black for Pem Fuel Cells. *Electrochim. Acta* **2006**, *51*, 4909−4915.

(2) Cho, C. Y.; Moon, J. H. Hierarchically Porous Tio2 Electrodes Fabricated by Dual Templating Methods for Dye-Sensitized Solar Cells. *Adv. Mater.* **2011**, *23*, 2971−2975.

(3) Reznik, C.; Landes, C. F. Transport in Supported Polyelectrolyte Brushes. *Acc. Chem. Res.* **2012**, *45*, 1927−1935.

(4) Yao, Y.; Czymmek, K. J.; Pazhianur, R.; Lenhoff, A. M. Three-Dimensional Pore Structure of Chromatographic Adsorbents from Electron Tomography. *Langmuir* **2006**, *22*, 11148−11157.

(5) Bruns, S.; Tallarek, U. Physical Reconstruction of Packed Beds and Their Morphological Analysis: Core−Shell Packings as an Example. *J. Chromatogr. A* **2011**, *1218*, 1849−1860.

(6) Hormann, K.; Müllner, T.; Bruns, S.; Höltzel, A.; Tallarek, U. Morphology and Separation Efficiency of a New Generation of Analytical Silica Monoliths. *J. Chromatogr. A* **2012**, *1222*, 46−58.

(7) Leinweber, F. C.; Tallarek, U. Chromatographic Performance of Monolithic and Particulate Stationary Phases: Hydrodynamics and Adsorption Capacity. *J. Chromatogr. A* **2003**, *1006*, 207−228.

(8) Kang, M. K.; Colombo, J. S.; D'Souza, R. N.; Hartgerink, J. D. Sequence Effects of Self-Assembling Multidomain Peptide Hydrogels on Encapsulated Shed Cells. *Biomacromolecules* **2014**, *15*, 2004−2011.

(9) Worthington, P.; Pochan, D. J.; Langhans, S. A. Peptide Hydrogels−Versatile Matrices for 3d Cell Culture in Cancer Medicine. *Front. Oncol.* **2015**, *5*, 92.

(10) Koetting, M. C.; Peters, J. T.; Steichen, S. D.; Peppas, N. A. Stimulus-Responsive Hydrogels: Theory, Modern Advances, and Applications. *Mater. Sci. Eng., R* **2015**, *93*, 1−49.

(11) Du, X.; Zhou, J.; Shi, J.; Xu, B. Supramolecular Hydrogelators and Hydrogels: From Soft Matter to Molecular Biomaterials. *Chem. Rev.* **2015**, *115*, 13165−13307.

(12) Kisley, L.; Serrano, K. A.; Guin, D.; Kong, X.; Gruebele, M.; Leckband, D. E. Direct Imaging of Protein Stability and Folding

Kinetics in Hydrogels. *ACS Appl. Mater. Interfaces* **2017**, *9*, 21606−21617.
(13) Kabanov, A. V.; Vinogradov, S. V. Nanogels as Pharmaceutical Carriers: Finite Networks of Infinite Capabilities. *Angew. Chem., Int. Ed.* **2009**, *48*, 5418−5429.
(14) Tarasova, I. A.; Masselon, C. D.; Gorshkov, A. V.; Gorshkov, M. V. Predictive Chromatography of Peptides and Proteins as a Complementary Tool for Proteomics. *Analyst* **2016**, *141*, 4816−4832.
(15) National Academies of Sciences, Engineering, and Medicine.*A Research Agenda for Transforming Separation Science*; The National Academies Press: Washington, DC, 2019; p 114.
(16) Avorn, J. The $2.6 Billion Pill—Methodologic and Policy Considerations. *N. Engl. J. Med.* **2015**, *372*, 1877−1879.
(17) Maharjan, P.; Woonton, B. W.; Bennett, L. E.; Smithers, G. W.; DeSilva, K.; Hearn, M. T. Novel Chromatographic Separation—the Potential of Smart Polymers. *Innovative Food Sci. Emerging Technol.* **2008**, *9*, 232−242.
(18) Bajpai, A.; Bajpai, J.; Saini, R.; Gupta, R. Responsive Polymers in Biology and Technology. *Polym. Rev.* **2011**, *51*, 53−97.
(19) Neamtu, I.; Rusu, A. G.; Diaconu, A.; Nita, L. E.; Chiriac, A. P. Basic Concepts and Recent Advances in Nanogels as Carriers for Medical Applications. *Drug Delivery* **2017**, *24*, 539−557.
(20) Lorenzo, R. A.; Carro, A. M.; Concheiro, A.; Alvarez-Lorenzo, C. Stimuli-Responsive Materials in Analytical Separation. *Anal. Bioanal. Chem.* **2015**, *407*, 4927−4948.
(21) Nguyen, B.; Claveau-Mallet, D.; Hernandez, L. M.; Xu, E. G.; Farner, J. M.; Tufenkji, N. Separation and Analysis of Microplastics and Nanoplastics in Complex Environmental Samples. *Acc. Chem. Res.* **2019**, *52*, 858−866.
(22) Tan, S.; Saito, K.; Hearn, M. T. Stimuli-Responsive Polymeric Materials for Separation of Biomolecules. *Curr. Opin. Biotechnol.* **2018**, *53*, 209−223.
(23) Susanto, H.; Ulbricht, M. Photografted Thin Polymer Hydrogel Layers on Pes Ultrafiltration Membranes: Characterization, Stability, and Influence on Separation Performance. *Langmuir* **2007**, *23*, 7818−7830.
(24) Tokarev, I.; Minko, S. Stimuli-Responsive Porous Hydrogels at Interfaces for Molecular Filtration, Separation, Controlled Release, and Gating in Capsules and Membranes. *Adv. Mater.* **2010**, *22*, 3446−3462.
(25) Maaloum, M.; Pernodet, N.; Tinland, B. Agarose Gel Structure Using Atomic Force Microscopy: Gel Concentration and Ionic Strength Effects. *Electrophoresis* **1998**, *19*, 1606−1610.
(26) Polarz, S.; Antonietti, M. Porous Materials Via Nanocasting Procedures: Innovative Materials and Learning About Soft-Matter Organization. *Chem. Commun.* **2002**, 2593−2604.
(27) Breedveld, V.; Pine, D. Microrheology as a Tool for High-Throughput Screening. *J. Mater. Sci.* **2003**, *38*, 4461−4470.
(28) Wöll, D.; Flors, C. Super-Resolution Fluorescence Imaging for Materials Science. *Small Methods* **2017**, *1*, 1700191.
(29) Saini, A.; Kisley, L. Fluorescence Microscopy of Biophysical Protein Dynamics in Nanoporous Hydrogels. *J. Appl. Phys.* **2019**, *126*, 081101.
(30) Ullal, C. K.; Schmidt, R.; Hell, S. W.; Egner, A. Block Copolymer Nanostructures Mapped by Far-Field Optics. *Nano Lett.* **2009**, *9*, 2497−2500.
(31) Ullal, C. K.; Primpke, S.; Schmidt, R.; Böhm, U.; Egner, A.; Vana, P.; Hell, S. W. Flexible Microdomain Specific Staining of Block Copolymers for 3d Optical Nanoscopy. *Macromolecules* **2011**, *44*, 7508−7510.
(32) Penwell, S. B.; Ginsberg, L. D.; Ginsberg, N. S. Bringing Far-Field Subdiffraction Optical Imaging to Electronically Coupled Optoelectronic Molecular Materials Using Their Endogenous Chromophores. *J. Phys. Chem. Lett.* **2015**, *6*, 2767−2772.
(33) Nevskyi, O.; Sysoiev, D.; Oppermann, A.; Huhn, T.; Wöll, D. Nanoscopic Visualization of Soft Matter Using Fluorescent Diarylethene Photoswitches. *Angew. Chem., Int. Ed.* **2016**, *55*, 12698−12702.
(34) Tian, Z.; Li, A. D. Q.; Hu, D. Super-Resolution Fluorescence Nanoscopy Applied to Imaging Core−Shell Photoswitching Nanoparticles and Their Self-Assemblies. *Chem. Commun.* **2011**, *47*, 1258−1260.
(35) Gramlich, M.; Bae, J.; Hayward, R.; Ross, J. Fluorescence Imaging of Nanoscale Domains in Polymer Blends Using Stochastic Optical Reconstruction Microscopy (Storm). *Opt. Express* **2014**, *22*, 8438−8450.
(36) Albertazzi, L.; van der Zwaag, D.; Leenders, C. M.; Fitzner, R.; van der Hofstad, R. W.; Meijer, E. Probing Exchange Pathways in One-Dimensional Aggregates with Super-Resolution Microscopy. *Science* **2014**, *344*, 491−495.
(37) ONeil, C. E.; Jackson, J. M.; Shim, S.-H.; Soper, S. A. Interrogating Surface Functional Group Heterogeneity of Activated Thermoplastics Using Super-Resolution Fluorescence Microscopy. *Anal. Chem.* **2016**, *88*, 3686−3696.
(38) Conley, G. M.; Nöjd, S.; Braibanti, M.; Schurtenberger, P.; Scheffold, F. Superresolution Microscopy of the Volume Phase Transition of Pnipam Microgels. *Colloids Surf., A* **2016**, *499*, 18−23.
(39) Gelissen, A. P.; Oppermann, A.; Caumanns, T.; Hebbeker, P.; Turnhoff, S. K.; Tiwari, R.; Eisold, S.; Simon, U.; Lu, Y.; Mayer, J. 3d Structures of Responsive Nanocompartmentalized Microgels. *Nano Lett.* **2016**, *16*, 7295−7301.
(40) Conley, G. M.; Aebischer, P.; Nöjd, S.; Schurtenberger, P.; Scheffold, F. Jamming and Overpacking Fuzzy Microgels: Deformation, Interpenetration, and Compression. *Science advances* **2017**, *3*, e1700969.
(41) Alvarez, L. H.; Eisold, S.; Gumerov, R. A.; Strauch, M.; Rudov, A. A.; Lenssen, P.; Merhof, D.; Potemkin, I. I.; Simon, U.; Wöll, D. Deformation of Microgels at Solid-Liquid Interfaces Visualized in Three-Dimension. *Nano Lett.* **2019**, *19*, 8862−8867.
(42) Shuang, B.; Chen, J.; Kisley, L.; Landes, C. F. Troika of Single Particle Tracking Programing: Snr Enhancement, Particle Identification, and Mapping. *Phys. Chem. Chem. Phys.* **2014**, *16*, 624−634.
(43) Kisley, L.; Brunetti, R.; Tauzin, L. J.; Shuang, B.; Yi, X.; Kirkeminde, A. W.; Higgins, D. A.; Weiss, S.; Landes, C. F. Characterization of Porous Materials by Fluorescence Correlation Spectroscopy Super-Resolution Optical Fluctuation Imaging. *ACS Nano* **2015**, *9*, 9158−9166.
(44) Lim, S.; Song, J. E.; La, J. A.; Cho, E. C. Gold Nanospheres Assembled on Hydrogel Colloids Display a Wide Range of Thermoreversible Changes in Optical Bandwidth for Various Plasmonic-Based Color Switches. *Chem. Mater.* **2014**, *26*, 3272−3279.
(45) Shen, H.; Tauzin, L. J.; Wang, W.; Hoener, B.; Shuang, B.; Kisley, L.; Hoggard, A.; Landes, C. F. Single-Molecule Kinetics of Protein Adsorption on Thin Nylon-6,6 Films. *Anal. Chem.* **2016**, *88*, 9926−9933.
(46) Han, F.; Soeriyadi, A. H.; Vivekchand, S.; Gooding, J. J. Simple Method for Tuning the Optical Properties of Thermoresponsive Plasmonic Nanogels. *ACS Macro Lett.* **2016**, *5*, 626−630.
(47) Parthasarathy, R. Rapid, Accurate Particle Tracking by Calculation of Radial Symmetry Centers. *Nat. Methods* **2012**, *9*, 724.
(48) Elliott, L. C.; Barhoum, M.; Harris, J. M.; Bohn, P. W. Trajectory Analysis of Single Molecules Exhibiting Non-Brownian Motion. *Phys. Chem. Chem. Phys.* **2011**, *13*, 4326−4334.
(49) Tauzin, L. J.; Shen, H.; Moringo, N. A.; Roddy, M. H.; Bothof, C. A.; Griesgraber, G. W.; McNulty, A. K.; Rasmussen, J. K.; Landes, C. F. Variable Surface Transport Modalities on Functionalized Nylon Films Revealed with Single Molecule Spectroscopy. *RSC Adv.* **2016**, *6*, 27760−27766.
(50) Moringo, N. A.; Shen, H.; Tauzin, L. J.; Wang, W.; Bishop, L. D.; Landes, C. F. Variable Lysozyme Transport Dynamics on Oxidatively Functionalized Polystyrene Films. *Langmuir* **2017**, *33*, 10818−10828.
(51) Dertinger, T.; Colyer, R.; Iyer, G.; Weiss, S.; Enderlein, J. Fast, Background-Free, 3d Super-Resolution Optical Fluctuation Imaging (Sofi). *Proc. Natl. Acad. Sci. U. S. A.* **2009**, *106*, 22287.

https://dx.doi.org/10.1021/acs.jpcb.0c01807
J. Phys. Chem. B XXXX, XXX, XXX−XXX

(52) Boening, D.; Groemer, T. W.; Klingauf, J. Applicability of an Em-Ccd for Spatially Resolved Tir-Ics. *Opt. Express* **2010**, *18*, 13516−13528.
(53) Pham, T. Q. *Non-Maximum Suppression Using Fewer Than Two Comparisons Per Pixel*; International Conference on Advanced Concepts for Intelligent Vision Systems; Springer, 2010; pp 438−451.
(54) Khan, F. An Initial Seed Selection Algorithm for K-Means Clustering of Georeferenced Data to Improve Replicability of Cluster Assignments for Mapping Application. *Appl. Soft Comput.* **2012**, *12*, 3698−3700.
(55) Pavan, K. K.; Rao, A. A.; Rao, A.; Sridhar, G. Robust Seed Selection Algorithm for K-Means Type Algorithms. *arXiv preprint arXiv:1202.1585* **2012**.
(56) Arthur, D.; Vassilvitskii, S. In K-Means++: The Advantages of Careful Seeding. *Proceedings of the eighteenth annual ACM-SIAM symposium on Discrete algorithms*; Society for Industrial and Applied Mathematics, 2007; pp 1027−1035.
(57) Ostrovsky, R.; Rabani, Y.; Schulman, L. J.; Swamy, C. The Effectiveness of Lloyd-Type Methods for the K-Means Problem. *J. Assoc. Comput. Mach.* **2012**, *59*, 28.
(58) Basu, S.; Banerjee, A.; Mooney, R. Semi-Supervised Clustering by Seeding. *Proceedings of 19th International Conference on Machine Learning (ICML-2002)*; Citeseer, 2002.
(59) McUmber, A. C.; Randolph, T. W.; Schwartz, D. K. Electrostatic Interactions Influence Protein Adsorption (but Not Desorption) at the Silica−Aqueous Interface. *J. Phys. Chem. Lett.* **2015**, *6*, 2583−2587.
(60) Nelson, N.; Schwartz, D. K. Specific Ion (Hofmeister) Effects on Adsorption, Desorption, and Diffusion at the Solid−Aqueous Interface. *J. Phys. Chem. Lett.* **2013**, *4*, 4064−4068.
(61) Ricka, J.; Tanaka, T. Swelling of Ionic Gels: Quantitative Performance of the Donnan Theory. *Macromolecules* **1984**, *17*, 2916−2921.
(62) Tcherniak, A.; Reznik, C.; Link, S.; Landes, C. F. Fluorescence Correlation Spectroscopy: Criteria for Analysis in Complex Systems. *Anal. Chem.* **2009**, *81*, 746−754.
(63) Wang, W.; Shen, H.; Shuang, B.; Hoener, B. S.; Tauzin, L. J.; Moringo, N. A.; Kelly, K. F.; Landes, C. F. Super Temporal-Resolved Microscopy (Strem). *J. Phys. Chem. Lett.* **2016**, *7*, 4524−4529.
(64) Wang, W.; Ye, F.; Shen, H.; Moringo, N. A.; Dutta, C.; Robinson, J. T.; Landes, C. F. Generalized Method to Design Phase Masks for 3d Super-Resolution Microscopy. *Opt. Express* **2019**, *27*, 3799−3816.
(65) Purohit, A.; Vandenberg, W.; Dertinger, T.; Wöll, D.; Dedecker, P.; Enderlein, J. Spatio-Temporal Correlation Super-Resolution Optical Fluctuation Imaging. *EPL* **2019**, *125*, 20005.

https://dx.doi.org/10.1021/acs.jpcb.0c01807
J. Phys. Chem. B XXXX, XXX, XXX−XXX